Volume 57
Number 82
21 October 2021
Pages 10649–10808

ChemComm

Chemical Communications

rsc.li/chemcomm

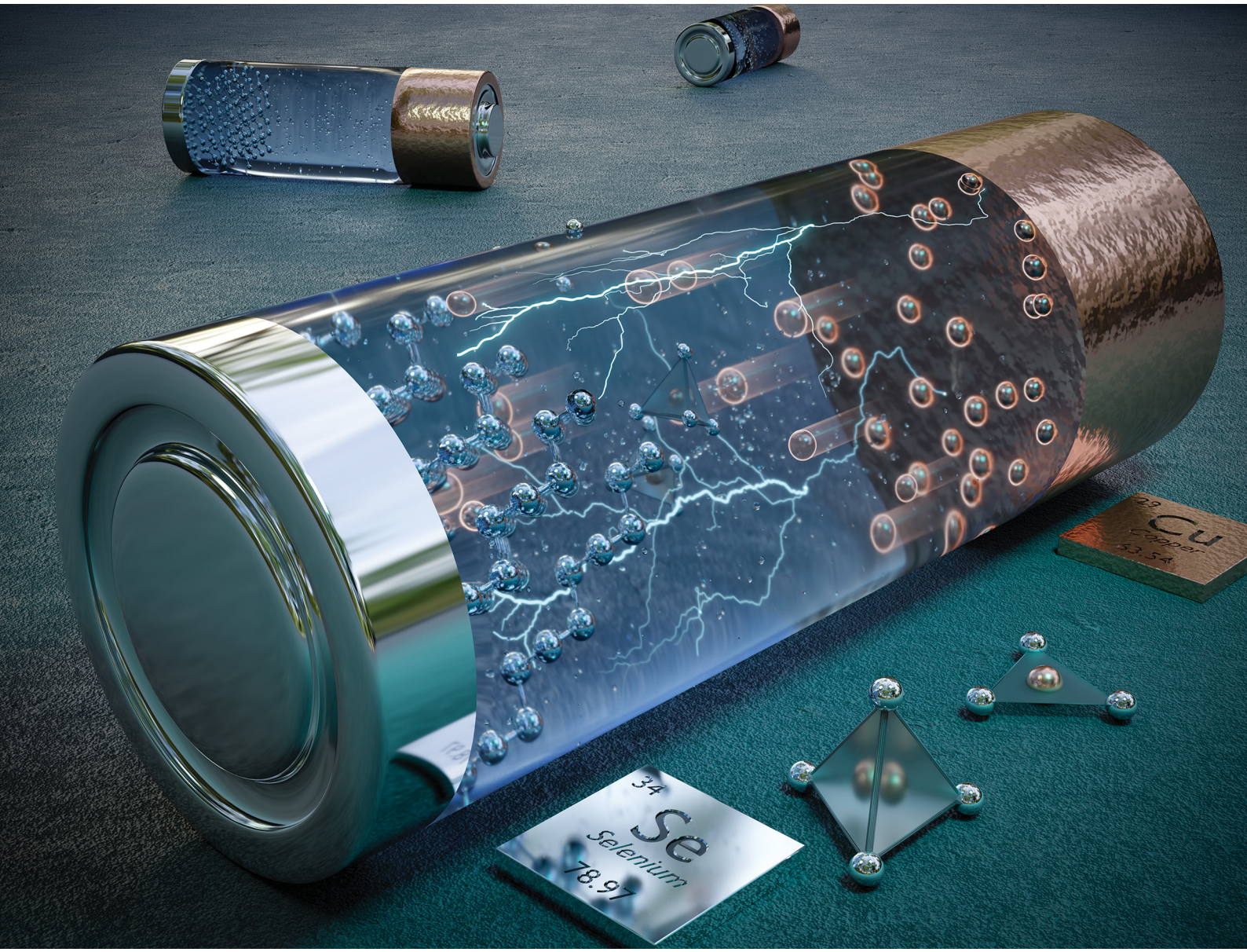

ISSN 1359-7345

ROYAL SOCIETY OF CHEMISTRY

COMMUNICATION

Zhenxing Feng, Xiulei Ji *et al.*

Reversible electrochemical conversion from selenium to cuprous selenide

ChemComm

COMMUNICATION

View Article Online
View Journal | View Issue

Cite this: *Chem. Commun.*, 2021, **57**, 10703

Received 22nd July 2021,
Accepted 9th September 2021

DOI: 10.1039/d1cc03983k

rsc.li/chemcomm

Reversible electrochemical conversion from selenium to cuprous selenide†

Sean K. Sandstrom,[a] Heng Jiang,[a] Marcos Lucero,[b] Yunkai Xu,[a] Trenton C. Gallagher,[a] Mengyuan Cao,[a] Zhenxing Feng *[b] and Xiulei Ji *[a]

Using elemental selenium as an electrode, the redox-active Cu^{2+}/Cu^{+} ion is reversibly hosted *via* the sequential conversion reactions of Se → CuSe → Cu_3Se_2 → Cu_2Se. The four-electron redox process from Se to Cu_2Se produces a high initial specific capacity of 1233 mA h g^{-1} based on the mass of selenium alone or 472 mA h g^{-1} based on the mass of Cu_2Se, the fully discharged product.

The need for effective grid-scale energy storage systems to store renewable energies and the rapid market growth of electric vehicles has spurred immense research into novel battery chemistries beyond Li-ion. Among these battery chemistries are those that use various cations, *e.g.*, Na^{+},[1,2] K^{+},[3] H^{+}/H_3O^{+},[4] Mg^{2+},[5] Ca^{2+},[6,7] Zn^{2+},[8,9] and Al^{3+},[10,11] and anions, *e.g.*, F^{-},[12] Cl^{-},[13] OH^{-},[14] NO_3^{-},[15] and superhalides,[16] as charge carriers. A common thread among these charge carriers is that they are usually redox inert when being transported through electrode host materials. On the other hand, ion charge carriers can undergo redox behaviors, while being hosted within an electrode material.[17–20] These so-called "redox-ion-charge-carrier" (RIC) electrodes have the potential benefits of attaining an additional capacity *via* the redox charge transfer of the inserted ions. Moreover, the RIC electrodes may allow for the studies of unique redox chemistries and electrosynthetic strategies of materials that are yet to be explored.

Herein, we demonstrate reversible hosting of a redox active Cu^{2+}/Cu^{+} charge carrier in a selenium (Se) electrode *via* the four-electron conversion of Se ↔ Cu_2Se. Benefiting from the higher electronic conductivity of selenium, the Cu–Se RIC electrode shows an exceedingly small extent of polarization roughly 40% that of the Cu–S electrode. Using *ex situ* X-ray diffraction (XRD), X-ray absorption spectroscopy (XAS), and energy dispersive X-ray spectroscopy (EDX) associated with transmission electron microscopy (TEM), the discharge/charge processes are found to proceed *via* a four-phase reaction mechanism of Se ↔ CuSe ↔ Cu_3Se_2 ↔ Cu_2Se, where half of the capacity is associated with the redox of Cu^{2+}/Cu^{+}. It is expected that the discharge process of this system may also be a valuable approach for the electrochemical synthesis of various nanoscale copper selenides, which could serve numerous applications.

Se is seen as a promising alternative to the more widely studied sulfur (S) electrodes due to the much higher electronic conductivity of semiconducting selenium (1×10^{-3} S m^{-1}) as compared to sulfur (5×10^{-28} S m^{-1}).[21–25] Although the specific capacity of a selenium cathode is lower than sulfur due to its higher atomic mass, the much higher density of selenium (4.81 g cm^{-3}) than sulfur (2.07 g cm^{-3}) can result in larger volumetric capacities for Se.

Following the pioneering work of other M–Se and M–S battery research, we prepared a nanocomposite by impregnating the micropores of Ketjenblack (KB) carbon with selenium *via* a typical melt-diffusion method (see ESI† for experimental details).[23,26] Fig. S1 (ESI†) shows the physical characterization of the composite with ~75 wt% Se (Se/KB-75), where the amorphous features of the XRD pattern indicate that the Se is well encapsulated within the nanopores of the KB. TEM images with associated EDX elemental mapping confirm the presence of nanoscale Se homogeneously distributed throughout the carbon matrix of the Se/KB-75 composite (Fig. 1). Through calculations, we found that ~88 wt% Se is the theoretical maximum Se content that can be encapsulated within the pores of KB and still allow for the full volume expansion associated with the formation of cuprous selenide, *i.e.*, Cu_2Se. Through experiments, however, a mass ratio of 80 wt% Se was found near the maximum selenium content that could be successfully incorporated into the KB pores as indicated by peaks corresponding to selenium in the XRD pattern of the 83 wt% composite (Fig. S2, ESI†).

To investigate the electrochemical Cu^{2+} storage behavior of the Se electrode, three-electrode cells were assembled consisting of

[a] *Department of Chemistry, Oregon State University, Corvallis, OR, 97331, USA. E-mail: david.ji@oregonstate.edu*
[b] *School of Chemical, Biological, and Environmental Engineering, Oregon State University, Corvallis, OR, 97331, USA. E-mail: zhenxing.feng@oregonstate.edu*

† Electronic supplementary information (ESI) available. See DOI: 10.1039/d1cc03983k

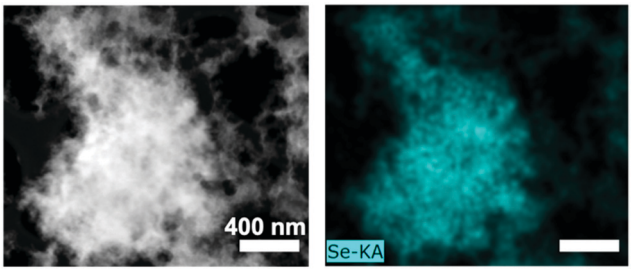

Fig. 1 High angle annular dark field scanning transmission electron microscopy (HAADF-STEM) image of the Se/KB-75 nanocomposite (left) with associated elemental mapping of the Se content (right).

the Se/KB-75 composite as the working electrode, 0.5 M aqueous $CuSO_4$ as the electrolyte, and metallic copper as the counter and reference electrodes. Fig. 2a shows the galvanostatic charge–discharge (GCD) potential profiles obtained at a current rate of 100 mA g^{-1} based on the mass of the selenium within the composite. The first cycle discharge capacity of 1233 mA h g^{-1} suggests a near-four-electron reduction based on the theoretical specific capacity of 1357 mA h g^{-1} for the conversion from Se to Cu_2Se. The less desirable GCD profiles obtained using the bulk Se electrode emphasize the significant benefits of forming a nanocomposite (Fig. S3a, ESI†). For the bulk Se electrode, the capacity is lower, yet still impressive (831 mA h g^{-1} for the first discharge), and there are three distinct plateaus in the GCD profiles. After forming a nanocomposite, the GCD profiles lose these distinct plateaus and show a single overarching slope due to the nano-sized active material (Fig. 2a). Cyclic voltammetry (CV) curves of the bulk Se electrode show three pairs of anodic and cathodic peaks, indicating a possible four-phase reaction mechanism

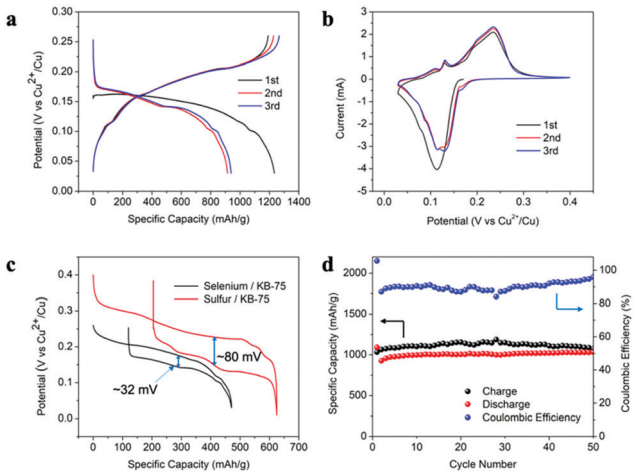

Fig. 2 Electrochemical performance of the Se/KB-75 composite electrode. (a) GCD potential profiles of the Se/KB-75 electrode obtained at a current rate of 100 mA g^{-1}. (b) CV curves of the Se/KB-75 at a scan rate of 0.03 mV s^{-1}. (c) Comparison of the second cycle GCD profiles of the Se/KB-75 and S/KB-75 composite electrodes, with specific capacities based on the fully discharged products (*i.e.*, Cu_2Se or Cu_2S), showing the considerably lower polarization of the Se/KB-75 electrode. (d) Cycling performance of the Se/KB-75 composite at 100 mA g^{-1}. All the current rate values are based on the mass of Se (or S) within the composites.

(Fig. S3b, ESI†). In contrast, CV curves of the Se/KB-75 nanocomposite display a pair of primary anodic and cathodic peaks at ~0.23 and ~0.12 V, respectively, which further corroborates the nano dimensions of the Cu–Se active mass of the composite electrode (Fig. 2b). Additionally, Fig. S4 (ESI†) shows the GCD potential profiles obtained using Se/KB composites with 66, 80, and 83 wt% Se. These potential profiles further highlight the benefit of confining Se within the KB pores, where the overpotential is considerably worse for the composite without complete Se incorporation (*e.g.*, Se/KB-83).

When compared to a sulfur (S/KB-75) composite electrode, the Se/KB-75 electrode shows a considerably reduced polarization and improved energy efficiency (Fig. 2c and Fig. S5, ESI†). The lower polarization suggests improved reaction kinetics stemming from the much higher electronic conductivity of Se as compared to S. Based on the mass of the fully discharged products, *i.e.*, Cu_2Se or Cu_2S, the Se electrode has a specific discharge capacity that is ~83% of the capacity seen for the S electrode (Fig. 2c). In terms of rate performance, the Se/KB-75 and S/KB-75 composites were found to be similar with ~87% and ~81% capacity retention, respectively, in going from a rate of 0.1C to 2C (Fig. S6, ESI†). The polarization increased by 49 and 83 mV for the Se and S electrodes, respectively, in changing from 0.1 to 2C. Moreover, despite the lower capacity of the selenium electrode, it should be noted that the much higher density of selenium (4.81 g cm^{-3} *vs.* 2.07 g cm^{-3} for sulfur) makes the Cu–S and Cu–Se electrode systems comparable in terms of volumetric energy metrics. The initial volumetric capacity of the Se electrode (5931 mA h cm^{-3}) is larger than that of the S electrode (5740 mA h cm^{-3}) based on the Se (or S) volume alone. However, based on the entire volume of the composites, it should be noted that the theoretical volumetric capacity is lower for the Se/KB-75 electrode (447.8 mA h cm^{-3}) than it is for the S/KB-75 electrode (1103 mA h cm^{-3}). The relatively low Coulombic efficiencies (CE) seen for the Cu–Se RIC electrode may be due to limited reversibility of the Cu–Se conversion reactions in the initial cycles before the electrode has been conditioned.

The Se/KB-75 composite also demonstrates excellent cycling stability (Fig. 2d). At a current rate of 100 mA g^{-1} (0.074C), the Se/KB-75 composite electrode can be cycled for over 50 cycles (~44 days) with 94% capacity retention from the first cycle discharge capacity (Fig. 2d). Although there is a drop in capacity after the first cycle, the discharge capacity progressively increases over the next 49 cycles. The CE also continues to improve during the 49 cycles, which suggests a continued activation process of the Se/KB-75 electrode. A similar activation process was observed while cycling the Se/KB-75 electrode at the higher current rates of 1 and 10 A g^{-1}, in which the capacity can be seen to steadily increase while cycling (Fig. S7, ESI†). At 1 A g^{-1}, the discharge capacity increases to a maximum of 848 mA h g^{-1} by the 219th cycle and then steadily decreases to 812 mA h g^{-1} by the 250th cycle (Fig. S7a, ESI†). This excellent cycling stability indicates the lack of soluble polyselenides formed during the reversible Cu–Se solid–solid conversion reactions. The higher electronic conductivity of

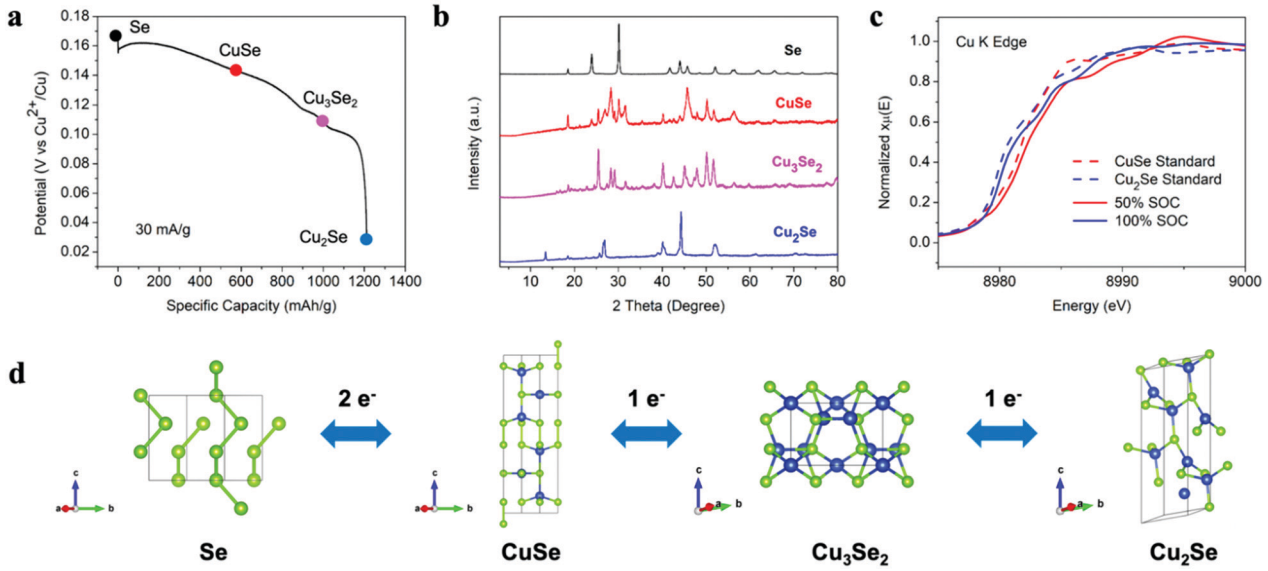

Fig. 3 Characterization of the cycling mechanism of the Cu–Se electrode. (a) Discharge profile of the Cu–Se free-standing film electrode with structural evolution marked at different SOC. (b) *Ex situ* XRD patterns corresponding to the different SOC. (c) Normalized XANES of the Cu K-edge spectra of the 50% and 100% SOC electrodes and the CuSe and Cu_2Se standards. (d) Schematic illustrating the conversion reactions that occur while cycling the Cu–Se RIC electrode. The green and blue spheres represent Se and Cu atoms, respectively.

selenium may result in superior cycling capability as compared to sulfur. Moreover, the lesser extent of volume change associated with the formation of cuprous selenides (*i.e.*, 63% volume increase from Se to Cu_2Se) as compared to the formation of cuprous sulfides (*i.e.*, 88% volume increase from S to Cu_2S) may allow the Cu–Se RIC electrode to experience less structural degradation while cycling.

To investigate how the structure changes during cycling, we conducted *ex situ* XRD on a Cu–Se free-standing film electrode, composed of bulk selenium physically mixed with conductive carbon, C65, at various states of charge (SOCs) (Fig. 3a and Fig. S8, ESI†). The color of each XRD curve in Fig. 3b corresponds to the SOC marked by the dot with the respective color on the discharge profile in Fig. 3a. Upon discharge, Se first converts to hexagonal CuSe at roughly 50% SOC. The resulting CuSe is then transformed to mixed valence Cu^{2+}/Cu^{+} (one Cu^{2+} and two Cu^{+}) umangite Cu_3Se_2 at 75% SOC and finally to monoclinic Cu_2Se at the end of the discharge process, *i.e.*, at 100% SOC, where each phase has been carefully indexed (Fig. 3b and Fig. S8, ESI†). These results are supported by Cu K-edge X-ray absorption near-edge structure (XANES) studies,[27–29] where the spectra of the half-discharged and fully discharged samples match well with the CuSe and Cu_2Se standards, respectively (Fig. 3c). Minor variations in the position and shape of the XANES spectra may be due to slight differences in the crystal structures (*e.g.*, symmetry and coordination) of the standards (chemically synthesized) and the Cu–Se electrodes (electrochemically synthesized) (Fig. S9, ESI†).[30] Interestingly, the spectrum obtained at ~75% SOC sits between the CuSe and Cu_2Se standards, which supports the mixed copper (2+/1+) valence of Cu_3Se_2 (Fig. S10a, ESI†). The linear combination fitting obtained using the CuSe and Cu_2Se standards matches well with the K-edge of the 75% SOC sample, further indicating the mixed Cu oxidation state of Cu_3Se_2 (Fig. S10b, ESI†). Based on these findings, Fig. 3d schematically illustrates the structural changes that occur at the Cu–Se RIC electrode during the (dis)charge process.

To further examine the structural evolution of the Cu–Se electrode during cycling, extended X-ray absorption fine structure (EXAFS) spectroscopy was conducted at the different SOC (Fig. 4 and Fig. S11, ESI†). The Fourier-transformed EXAFS spectra of the electrodes at 50% and 100% SOC match well with the spectra of the CuSe and Cu_2Se standards, respectively. The results of EXAFS indicate similar Cu–Se bond distances between the electrochemically formed samples and the standards. Moreover, by performing model-based fitting, the quantitative analysis of the electrode samples and their respective

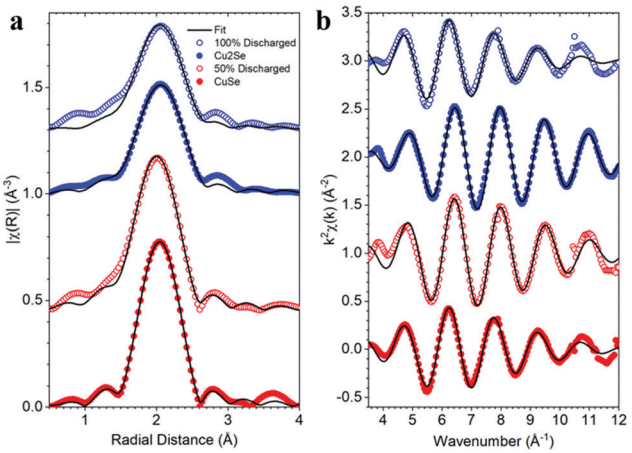

Fig. 4 Model based fitting of (a) Fourier-transformed and (b) k-space EXAFS spectra for the 50% and 100% SOC Cu–Se electrodes and the CuSe and Cu_2Se standards.

standards reveals similar coordination numbers and Cu–Se bond distances (Fig. 4 and Fig. S11, Table S1, ESI†). Similarly, the Cu–Se electrode at 75% SOC has a similar bond length and coordination to the predicted crystal structure of Cu_3Se_2, providing further evidence for the formation of tetragonal Cu_3Se_2.

EDX-TEM further confirms that Cu is inserted into the Se/KB-75 nanocomposite structure during the discharge process, where Cu can clearly be seen associated with Se in the fully discharged sample (Fig. S9, ESI†). It should also be noted that this electrochemical insertion of copper may be useful in forming various nanoscale copper selenides, which could be useful in a number of applications, such as battery electrodes,[31] thermoelectrics,[32] and photocatalysts.[33]

In conclusion, we have investigated the reversible hosting of a redox-active copper charge carrier in a selenium electrode. The Cu–Se RIC electrode demonstrates a four-electron transfer mechanism *via* the reversible conversion of Se to Cu_2Se with a high initial discharge capacity of 1233 mA h g^{-1}. Through *ex situ* XRD, XANES, and EXAFS analyses, we reveal the reaction pathway to occur *via* the sequential conversion reactions of Se ↔ CuSe ↔ Cu_3Se_2 ↔ Cu_2Se. Owing to the higher conductivity of Se, the Cu–Se RIC electrode shows considerably lower polarization and improved cycling stability than the analogous Cu–S RIC electrode. This study provides an example of the possibility of hosting new redox active charge carriers in selenium electrodes.

X. J. is grateful for the financial support from the U.S. National Science Foundation (NSF), Award No. CBET-1551693. Z. F. thanks NSF for the Award No. CBET-2016192. The authors thank Dr. Peter Eschbach and the Oregon State University Electron Microscopy Facility for STEM and EDX mapping measurements and Dr. Ryan Davis at SSRL for assistance with XAS measurements. Use of the Stanford Synchrotron Radiation Lightsource, SLAC National Accelerator Laboratory, is supported by the U.S. Department of Energy, Office of Science, Office of Basic Energy Sciences under Contract No. DE-AC02-76SF00515.

Conflicts of interest

There are no conflicts to declare.

Notes and references

1 M. D. Slater, D. Kim, E. Lee and C. S. Johnson, *Adv. Funct. Mater.*, 2013, **23**, 947–958.
2 S. Y. Hong, Y. Kim, Y. Park, A. Choi, N.-S. Choi and K. T. Lee, *Energy Environ. Sci.*, 2013, **6**, 2067–2081.
3 A. Eftekhari, *J. Power Sources*, 2004, **126**, 221–228.
4 Y. Xu, X. Wu and X. Ji, *Small Struct.*, 2021, **2**, 2000113.
5 H. Dong, O. Tutusaus, Y. Liang, Y. Zhang, Z. Lebens-Higgins, W. Yang, R. Mohtadi and Y. Yao, *Nat. Energy*, 2020, **5**, 1043–1050.
6 A. Ponrouch, C. Frontera, F. Bardé and M. R. Palacín, *Nat. Mater.*, 2016, **15**, 169–172.
7 A. L. Lipson, B. Pan, S. H. Lapidus, C. Liao, J. T. Vaughey and B. J. Ingram, *Chem. Mater.*, 2015, **27**, 8442–8447.
8 C. Xu, B. Li, H. Du and F. Kang, *Angew. Chem.*, 2012, **124**, 957–959.
9 L. E. Blanc, D. Kundu and L. F. Nazar, *Joule*, 2020, **4**, 771–799.
10 M.-C. Lin, M. Gong, B. Lu, Y. Wu, D.-Y. Wang, M. Guan, M. Angell, C. Chen, J. Yang, B.-J. Hwang and H. Dai, *Nature*, 2015, **520**, 324–328.
11 N. Jayaprakash, S. Das and L. Archer, *Chem. Commun.*, 2011, **47**, 12610–12612.
12 M. A. Reddy and M. Fichtner, *J. Mater. Chem.*, 2011, **21**, 17059–17062.
13 X. Zhao, S. Ren, M. Bruns and M. Fichtner, *J. Power Sources*, 2014, **245**, 706–711.
14 G. Karkera, M. A. Reddy and M. Fichtner, *J. Power Sources*, 2020, **481**, 228877.
15 H. Jiang, Z. Wei, L. Ma, Y. Yuan, J. J. Hong, X. Wu, D. P. Leonard, J. Holoubek, J. J. Razink, W. F. Stickle, F. Du, T. Wu, J. Lu and X. Ji, *Angew. Chem., Int. Ed.*, 2019, **58**, 5286–5291.
16 S. K. Sandstrom, X. Chen and X. Ji, *Carbon Energy*, 2021, **3**, 627–653.
17 X. Wu, A. Markir, L. Ma, Y. Xu, H. Jiang, D. P. Leonard, W. Shin, T. Wu, J. Lu and X. Ji, *Angew. Chem.*, 2019, **131**, 12770–12775.
18 J. J. Hong, L. Zhu, C. Chen, L. Tang, H. Jiang, B. Jin, T. C. Gallagher, Q. Guo, C. Fang and X. Ji, *Angew. Chem.*, 2019, **131**, 16057–16062.
19 C. Yang, J. Chen, X. Ji, T. P. Pollard, X. Lü, C.-J. Sun, S. Hou, Q. Liu, C. Liu, T. Qing, Y. Wang, O. Borodin, Y. Ren, K. Xu and C. Wang, *Nature*, 2019, **569**, 245–250.
20 Y. Wang, D. Chao, Z. Wang, J. Ni and L. Li, *ACS Nano*, 2021, **15**, 5420–5427.
21 A. Eftekhari, *Sustainable Energy Fuels*, 2017, **1**, 14–29.
22 X. Gu, T. Tang, X. Liu and Y. Hou, *J. Mater. Chem. A*, 2019, **7**, 11566–11583.
23 A. Abouimrane, D. Dambournet, K. W. Chapman, P. J. Chupas, W. Weng and K. Amine, *J. Am. Chem. Soc.*, 2012, **134**, 4505–4508.
24 Y. Cui, A. Abouimrane, C.-J. Sun, Y. Ren and K. Amine, *Chem. Commun.*, 2014, **50**, 5576–5579.
25 Y. Cui, A. Abouimrane, J. Lu, T. Bolin, Y. Ren, W. Weng, C. Sun, V. A. Maroni, S. M. Heald and K. Amine, *J. Am. Chem. Soc.*, 2013, **135**, 8047–8056.
26 X. Ji, K. T. Lee and L. F. Nazar, *Nat. Mater.*, 2009, **8**, 500–506.
27 M. Wang, L. Árnadóttir, Z. J. Xu and Z. Feng, *Nano-Micro Lett.*, 2019, **11**, 1–18.
28 M. Lucero, S. Qiu and Z. Feng, *Carbon Energy*, 2021, DOI: 10.1002/cey2.131.
29 Z. Feng, *Reference Module in Earth Systems and Environmental Sciences*, 2021, pp. 1–13.
30 M. Wang and Z. Feng, *Curr. Opin. Electrochem.*, 2021, 100803.
31 Y. Yang, J. Xiao, J. Cai, G. Wang, W. Du, Y. Zhang, X. Lu and C. C. Li, *Adv. Funct. Mater.*, 2021, **31**, 2005092.
32 M. Li, D. L. Cortie, J. Liu, D. Yu, S. M. K. N. Islam, L. Zhao, D. R. Mitchell, R. A. Mole, M. B. Cortie, S. Dou and X. Wang, *Nano Energy*, 2018, **53**, 993–1002.
33 M. Nouri, N. Zare-Dehnavi, F. Jamali-Sheini and R. Yousefi, *Colloids Surf., A*, 2020, **586**, 124196.

